Polymer 50 (2009) 1497–1504

Contents lists available at ScienceDirect

Polymer

journal homepage: www.elsevier.com/locate/polymer

Anomalous molecular orientation of isotactic polypropylene sheet containing *N*,*N*′-dicyclohexyl-2,6-naphthalenedicarboxamide

Masayuki Yamaguchi [a,*], Takashi Fukui [a], Kenzo Okamoto [a], Shintaro Sasaki [b], Yohei Uchiyama [a,c], Chiaki Ueoka [c]

[a] School of Materials Science, Japan Advanced Institute of Science and Technology, 1-1 Asahidai, Nomi, Ishikawa 923-1292, Japan
[b] Center for Nano Materials and Technology, Japan Advanced Institute of Science and Technology, 1-1 Asahidai, Nomi, Ishikawa 923-1292, Japan
[c] New Japan Chemical Co., Ltd., 13 Yoshijima, Yaguracho, Fushimi, Kyoto 612-8224, Japan

ARTICLE INFO

Article history:
Received 19 October 2008
Received in revised form
7 January 2009
Accepted 12 January 2009
Available online 20 January 2009

Keywords:
Polypropylene
Structure–property relations
X-ray diffraction

ABSTRACT

Small amount of *N*,*N*′-dicyclohexyl-2,6-naphthalenedicarboxamide as a β-form nucleating agent is dissolved beyond 280 °C in a molten isotactic polypropylene (iPP) and appears as needle crystals around at 240 °C during cooling procedure. Further, iPP molecules crystallize on the surface of the needle crystals, in which *c*-axis of the β-form iPP crystals grows perpendicular to the long axis of the needle crystals. Under flow field at extrusion processing, the needle crystals orient to the flow direction prior to the crystallization of iPP. As a result, *c*-axis of the β-form iPP crystals orients perpendicular to the applied flow direction with a small amount of α-form iPP. Moreover, the vertical molecular orientation of the extruded sheet sample is responsible for unique mechanical anisotropy; the fracture occurs along the transversal direction.

1. Introduction

Recently, considerable attention has been focused on the preparation of β crystalline form for isotactic polypropylene (iPP), although conventional processing operation provides the most stable α crystalline form with a sporadic occurrence of β-form. The β crystalline form was firstly identified in 1959 by Keith and Padden [1], who classified the crystalline modalities of iPP, for the sample quenched below 128 °C. Later, Tuner-Jones et al. reported that high content of β-form is observed in a sample with a mixture of water and glycerine by quenching at 100–120 °C [2]. Since then, several methods were proposed to generate β-form, as summarized in a review paper by Varga [3], such as doping nucleating agents [3–24], directional crystallization in a temperature-gradient field [25–27], shear-induced crystallization [28–31], and vibration induced crystallization [32].

In particular, the most effective way to obtain the samples containing predominantly β-form would be the addition of specific nucleating agents, as well known for *trans*-quinacridone discovered by Leugering [4]. Up to now, several nucleating agents for β modification have been reported, such as various pigments including *trans*-quinacridone [4–8], a mixture of pimelic acid and calcium stearate [9], calcium salts of pimelic and suberic acid [10,11], and *N*,*N*′-dicyclohexyl-2,6-naphthalenedicarboxamide [12–24].

The commercialization of *N*,*N*′-dicyclohexyl-2,6-naphthalenedicarboxamide, designated as NU-100 in this paper, from New Japan Chemical has a great impact on the research and development of β-form iPP in industries, because NU-100 has various attractive properties such as thermal stability and effective β nucleating ability. Crystallization kinetics and morphology observation of iPP containing NU-100 were carried out by several researchers. Kotek et al. revealed that the concentration should be more than 300 ppm to show the effective β nucleating ability [18,19], which was also supported by Menyhard et al. [22]. Although NU-100 acts as a very efficient β nucleator beyond the critical concentration [17], the selectivity is slightly poorer than that for *trans*-quinacridone and calcium salt of suberic and pimelic acid [22]. Further, the poor selectivity is responsible for dual nucleating ability, i.e. both α and β modifications simultaneously, as demonstrated by Varga and Menyhard by means of precise thermal analysis with polarized microscope observation [24]. Furthermore, they also showed that NU-100 appears in a molten iPP as needle crystals which grow with a lot of branch points [24].

Kawai et al. studied the crystalline structure of NU-100 in detail and proposed the epitaxial matching with iPP crystals [13,14]. According to them, *b*-axis of NU-100 is parallel to *c*-axis of iPP.

* Corresponding author. Tel.: +81 761 51 1621; fax: +81 761 51 1625.
E-mail address: m_yama@jaist.ac.jp (M. Yamaguchi).

0032-3861/$ – see front matter © 2009 Elsevier Ltd. All rights reserved.
doi:10.1016/j.polymer.2009.01.033

Finally, Zhou et al. [20] and Hou et al. [21] concluded by AFM observation that iPP lamellae grow perpendicular to the surface of the nucleating agent, suggesting the epitaxial growth of iPP.

From the view point of mechanical properties, it has been recognized that the presence of β crystalline form leads to enhanced toughness and higher drawability, but lower stiffness and yield stress [3,12,15,33–41]. In particular, great attention has been focused on the enhanced toughness for the industrial application, because fracture of α-form iPP occurs in a brittle manner. The marked toughness is attributed to the energy dissipation during the yield process due to the phase transformation from β to α form. Further, the deformation mechanism has been studied in detail as compared with α-form iPP. Karger-Kocsis demonstrated that plastic work term is 3–4 times higher for β-form iPP than that for α-form PP, based on "essential work of fracture concept" of the ductile fracture mechanism [35–37].

The peculiar lamellar morphology of β-form iPP would be the origin of the difference in the deformation mechanism [3]. Huy et al. studied the deformation mechanism of α and β-form iPP by means of simultaneous measurements of a stress–strain curve and an infra-red dichroic ratio [39]. They revealed that the α-form iPP prefers intra-lamellar slippage whereas inter-lamellar slippage is a dominant mechanism for the β-form iPP. The mechanism was supported by Lezak et al. by their XRD study employing the sample deformed under plane-strain compression [40]. Moreover, Li et al. investigated the deformation mechanism by an electron microscopic method [38]. They proved that crazing, not yielding, is the dominant cause of the fracture in the case of β-form iPP. Then the microcrazes are connected together and developed into large cracks. Furthermore, Chu et al. also reported that a number of pores appear during stretching of β-form iPP [12].

In this study, the molecular orientation of iPP containing NU-100 as well as the crystalline form is investigated in detail employing sheet samples extruded from a conventional T-die. In general, addition of a nucleating agent enhances the molecular orientation because of the rapid solidification. This phenomenon is pronounced in the case of a fibrous nucleating agent such as a sorbitol-derivative that is often called as a clarifier, as reported by Tenma and Yamaguchi [41] and Tenma et al. [42]. Since NU-100 also appears as needle crystals, the molecular orientation of iPP would be greatly influenced.

2. Experimental

2.1. Materials

Commercially available isotactic polypropylene (iPP) produced by Ziegler–Natta catalyst was used in this study. The melt flow rate is 10 [g/10 min] at 230 °C. Since the sample is a propylene homopolymer, the melting point measured by a differential scanning calorimeter at a heating rate of 10 °C/min is approximately 165 °C. Further, *N*,*N*′-dicyclohexyl-2,6-naphthalenedicarboxamide (New

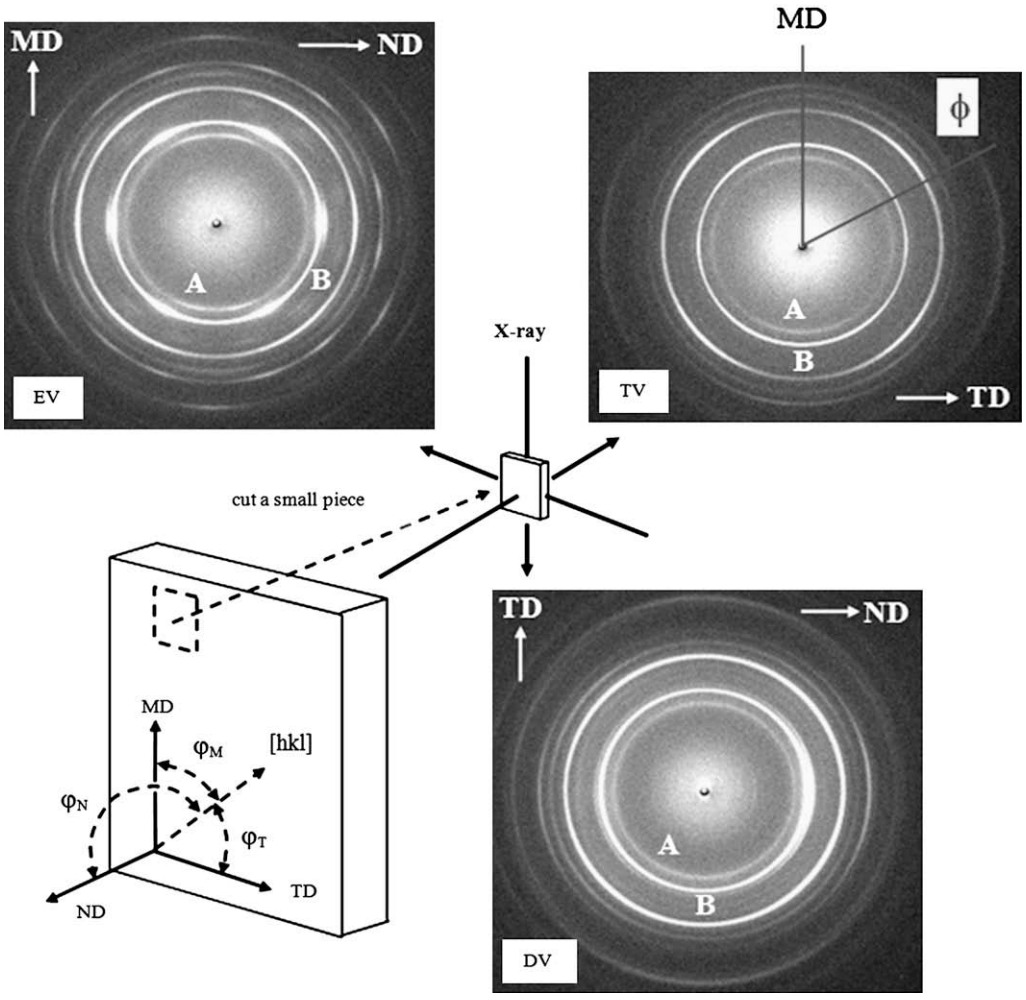

Fig. 1. XRD geometry for the extruded iPP sheet.

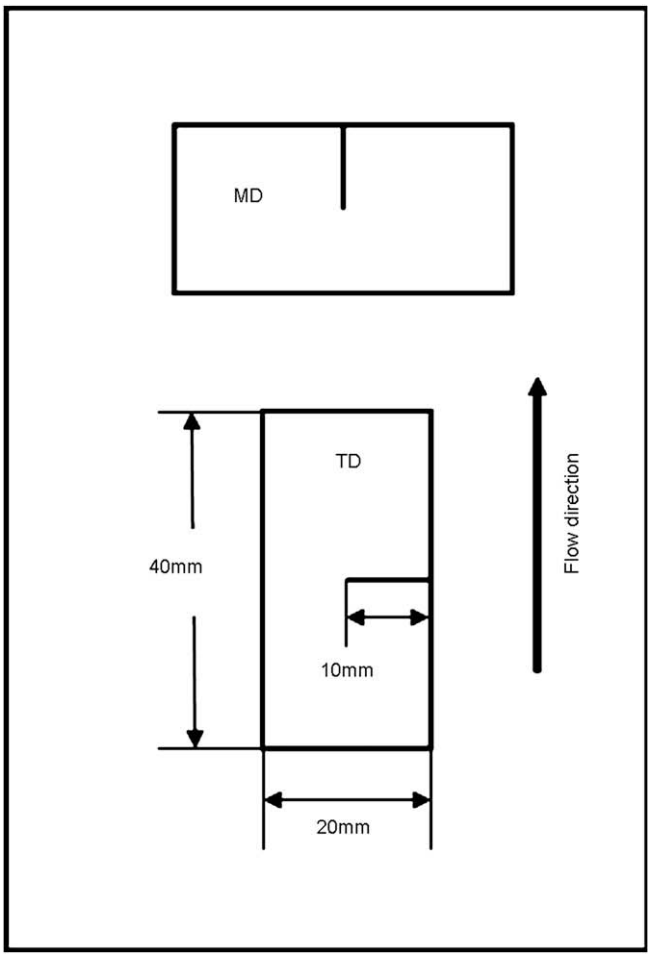

Fig. 2. Sample dimension for tear experiments.

Japan Chemical, NJ Star^{TR} NU-100), referred as NU-100, was employed without further purification.

2.2. Sample preparation

Firstly, iPP and NU-100 were mixed together with calcium stearate as an acid scavenger and thermal stabilizers such as a hindered phenol (Ciba, Irganox1010) and a phosphate (Ciba, Irgafos168). The concentrations of NU-100 were 500, 1000, and 2000 ppm. The amount of the acid scavenger and each thermal stabilizer used in the preparation were 0.05%. Compounding was performed by a co-rotating twin-screw extruder (Technovel, KZW 15TW-45MG-NH) at a screw rotation speed of 250 rpm. The temperature in the extruder and the die was controlled at either 280 °C or 200 °C. The strands extruded from the extruder were immediately quenched in a water bath and then cut by a strand cutter. The reference sample of PP was also prepared by the identical method without the addition of NU-100.

Secondly, the obtained pellets containing 500 ppm of NU-100, which were mixed at 280 °C, were fed into a single-screw extruder having a T-die controlled at 200 °C to obtain an extruded sheet with a thickness of 200 μm. The temperature of the chill-roll was controlled at 105 °C to enhance the β crystallization. The sample employed for the extrusion contains 500 ppm of NU-100. Further, pure iPP without NU-100 was also processed to obtain a reference sheet sample.

2.3. Measurements

Dissolution and crystallization behaviors of NU-100 in a molten iPP as well as the crystallization of iPP were evaluated by an optical microscope (Leica, DMLP) equipped with an automated hot-stage (Mettler, FP82HT). After heating from room temperature to 200 °C immediately, the sample was subsequently heated at a constant rate of 5 °C/min to 300 °C. Then the sample was cooled at a rate of 5 °C/min to 135 °C and then kept at the temperature. Birefringence of the sheet samples was measured by the optical microscope (Leica, DMLP) with a tilting compensator (Leica, Tilting Compensator B). Thin film specimens with a thickness of 2.5 μm were prepared at −100 °C by using an ultra microtome (Leica, FCS).

Wide-angle X-ray diffraction (WAXD) patterns were measured by using a graphite-monochromatized Cu Kα radiation beam focused via 0.3-mm pinhole collimator with a flat $20 \times 20\ cm^2$ imaging plate (IP) detector of 1900×1900 pixels (Rigaku, R-AXIS IIc). A small piece of the sample with edge sizes less than 1 mm was mounted with the sample-IP distance 10 cm. As is shown in Fig. 1, the exposure was performed with 7 min a shot in three geometrical conditions by directing the X-ray beam in the normal direction (ND) (through view: TV), in the transverse direction (TD) (edge view: EV), and in the machine direction (MD) (end view: DV). For the profile analysis, the crude intensity data recorded on IP were transformed into the curve (vs. the diffraction angle 2θ) corresponding to that measured with a conventional powder diffractometer, by correcting for the various effects, such as the dark noises of the IP system, the intensity decrease dependent inversely on square distance from the sample to each pixel, the oblique incidence of the diffracted light onto IP, and the air scattering. In the data files, two bytes were allotted to save each pixel intensity, and by bit-shift storage technique the maximum recording intensity was $8 \times 7FFF$ (hexadecimal) = 262,136 in the range of the linear sensitivity. All the treatments of the IP data were carried out with PC computers.

Mechanical anisotropy was evaluated by a tear test following ISO 6383-1 Trouser tear method using a tensile machine (Tokyo Testing Machine, Little Senster) at room temperature. The sample specimens were cut out from the sheet as shown in Fig. 2. The stretching rate was 10 mm/min. The tear-propagation resistance, defined as the force divided by the sample thickness, was measured as a function of the displacement of the crossheads.

3. Results and discussion

3.1. Dissolution and crystallization of NU-100

Dissolution and crystallization behavior of NU-100 in a molten iPP was evaluated employing pellet samples. Fig. 3 shows the optical micrographs for iPP containing 2000 ppm of NU-100. There are a lot of particles in the sample mixed at the lower temperature, i.e. 200 °C, even after melting of iPP, as seen in Fig. 3(a). The diameter of the particles is approximately 10 μm. The particles are dissolved into the molten iPP gradually at a heating process and disappear completely at 280 °C. On the contrary, the sample mixed at 280 °C shows homogeneous structure at 200 °C (Fig. 3(d)). As increasing the temperature, however, needle crystals appear in the molten iPP (Fig. 3(e)). The needle crystals of NU-100 grow until 250 °C, and then they are dissolved at 280 °C (Fig. 3(g)) as similar to the sample mixed at 200 °C. The results demonstrate that the dissolution of NU-100 occurs at 280 °C for the concentration, which is independent of the shape of NU-100. Moreover, it is confirmed that phase separation is not detected after dissolving NU-100 in a molten iPP.

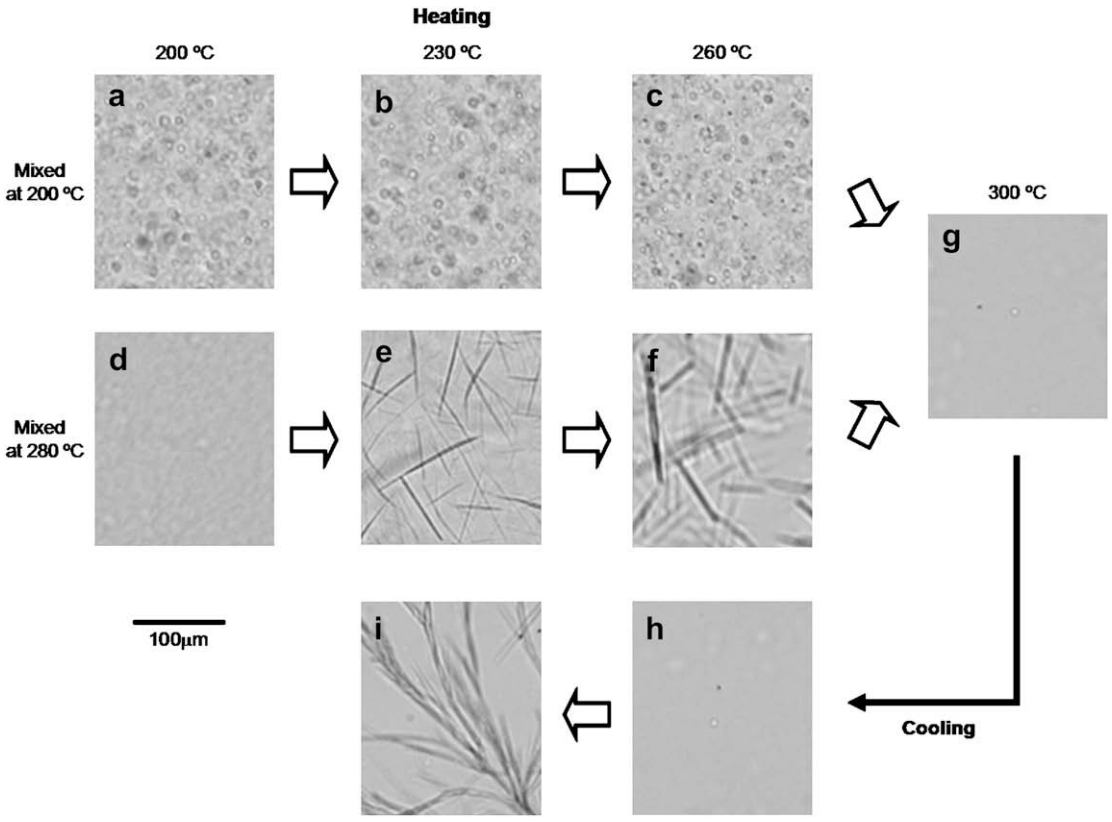

Fig. 3. Optical micrographs for iPP containing 2000 ppm of NU-100 at various temperatures: (a)–(c) mixed at 200 °C and (d)–(i) mixed at 280 °C: (a)–(g) heating process at a rate of 5 °C/min and (g)–(i) cooling process at a rate of 5 °C/min; (a) and (d) at 200 °C, (b), (e), and (i) at 230 °C, (c), (f), and (h) at 260 °C, and (g) at 300 °C.

During the cooling process from 300 °C, the needle crystals appear approximately at 240 °C and grow with branching as similar to the recent study [23] (Fig. 3(i)). Further, NU-100 is not detected at 260 °C at the cooling process, although they are not dissolved completely at the temperature at the heating process. In other words, there is the difference between dissolution and crystallization temperatures. This is reasonable, because it takes some time for NU-100 to crystallize in viscous iPP molecules especially near the dissolution temperature. In the case of the pure NU-100, not in a molten iPP, both the melting and crystallization temperatures are approximately 385 °C.

The temperatures of the dissolution and crystallization of NU-100 in a molten iPP were plotted as a function of the concentration in Fig. 4. As shown in the figure, the dissolution and crystallization occur at high temperature with increasing the concentration.

Fig. 5 shows the optical micrograph under crossed polars inserting a full-wave plate that adds 530 nm to an optical path. The sample containing 500 ppm of NU-100 is cooled down from 300 °C. The left figure shows the needle crystals of NU-100 appeared in a molten iPP at 210 °C. The diameter is approximately 10 μm and the length is 100–200 μm. As shown in the figure, the crystals whose long axis orients to northwest–southeast are blue, while those orient to northeast–southwest are yellow. This result indicates that the refractive index of the long axis is smaller than that of the short axis. Further, crystallization of iPP occurs at lower temperature on the needle crystals as shown in the right figure. It is apparent that iPP crystal exhibits the same color as the needle crystals. Considering that the refractive index of *c*-axis (fiber axis) is larger than those of the others for iPP, *c*-axis of iPP orients perpendicular to the long axis of the needle crystals, i.e. normal direction of the surface. Although the reason is unknown, the growth direction of iPP chains on NU-100, detected in the present study, is different from that proposed by Kawai et al. [13,14]. Further investigation on the precise characterization on the surface of NU-100 crystals will be required to clarify the possibility of epitaxial matching. Finally, it should be mentioned that spherulite texture is not detected at the present study, because the needle crystals, as nucleating agents, are too crowded to form spherulites, as similar to iPP containing a sorbitol derivative as a fibrous nucleator [41,42].

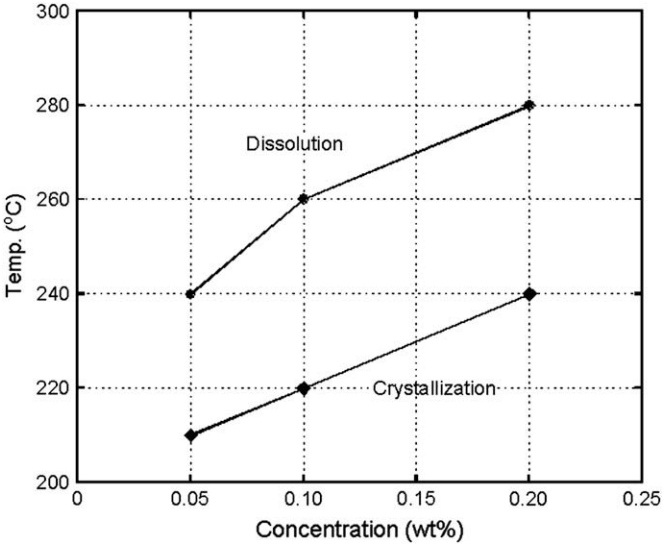

Fig. 4. Morphology map for iPP containing NU-100.

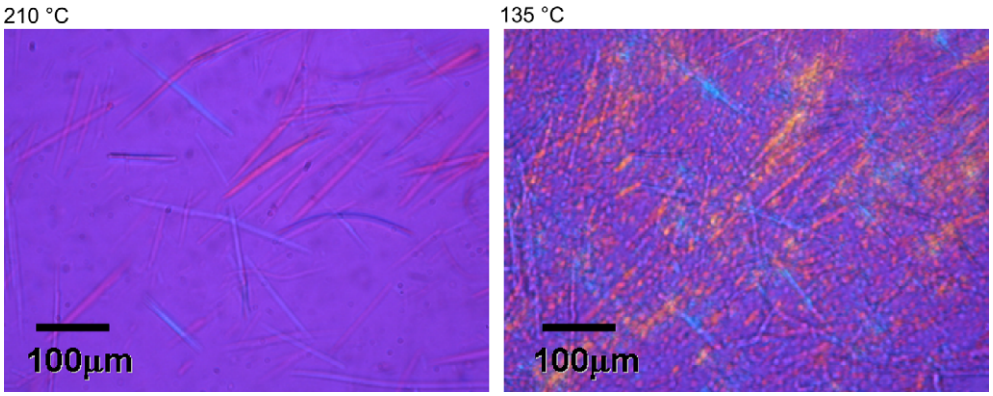

Fig. 5. Optical micrographs under crossed polars inserting a full-wave plate; (left) at 210 °C and (right) at 135 °C.

3.2. Structure of extruded sheet

Prior to the characterization of molecular orientation and crystalline form of iPP in the sheet samples, the dispersion state of the needle crystals in the sheet is examined. For the purpose of the observation, a small part of the sheet is placed between cover glasses in a hot stage and heated up to 170 °C without pressure. Fig. 6 shows the optical micrograph of the sheet sample, which is taken immediately after melting of iPP. It is confirmed that the needle crystals of NU-100 orient to the flow direction.

For the information on the orientation direction of iPP molecules, the magnitude of birefringence in the sheet samples was evaluated employing two slices from each sample as shown in Fig. 7. Further, the optical micrograph under crossed polars inserting a full-wave plate for a sliced sample is exemplified in Fig. 7. It is found from the birefringence measurement that $\Delta n(=n_{TD}-n_{ND})$ of the TD sample which is shown in the figure is 1.2×10^{-3}, and $\Delta n(=n_{MD}-n_{ND})$ of the MD sample is 7.5×10^{-4}. The result demonstrates that iPP molecules orient perpendicular to the flow direction, i.e. $n_{MD}-n_{TD}=-4.5\times10^{-4}$, which is an extraordinary orientation. Considering that the intrinsic birefringences of α-form crystal, smectic-form, and amorphous region are 4.2×10^{-2}, 4.0×10^{-2}, and 3.8×10^{-2}, respectively [43,44], the orientation function of the sheet would be around −0.01. We are currently characterizing the orientation function quantitatively [45]. As a comparison, the birefringence of the extruded sheet of pure iPP is also examined. Consequently, the *c*-axis of iPP is found to orient to the flow direction slightly; Δn_{TD-ND} is smaller than Δn_{MD-ND}, suggesting iPP chains orient to the flow direction, i.e. ordinary orientation, which will be demonstrated in detail by XRD analysis.

For the better understanding of the molecular orientation as well as polymorphism, XRD measurements were carried out for the sheet sample containing NU-100. The XRD patterns reveal that the extruded iPP sheet comprises both the α- and β-forms and the latter is much predominant. Fig. 8 exhibits the assignments of the reflections in the EV pattern, in which the α reflections are shown in the left side and the β reflections are in the right side.

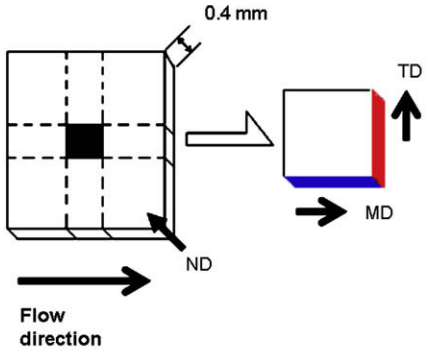

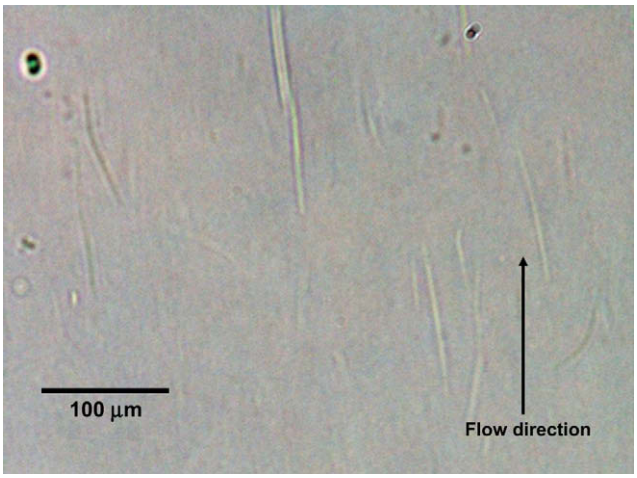

Fig. 6. Optical micrograph for extruded iPP sheet containing 500 ppm of NU-100. The sample was heated to 200 °C to melt iPP. The arrow in the figure indicates the flow direction (MD).

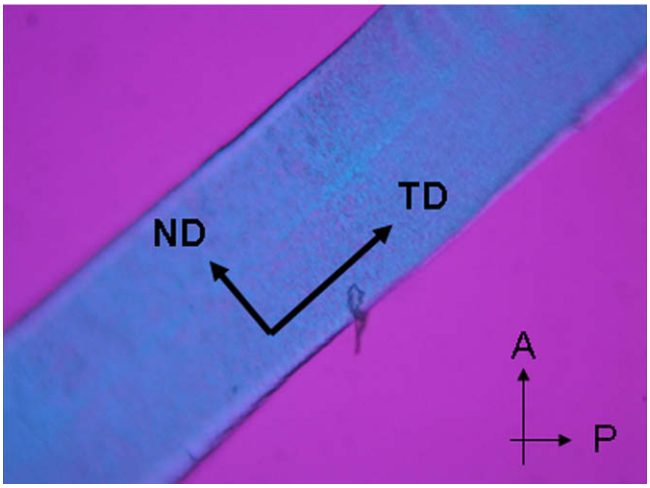

Fig. 7. Optical micrograph with a wave plate for extruded iPP containing 500 ppm of NU-100.

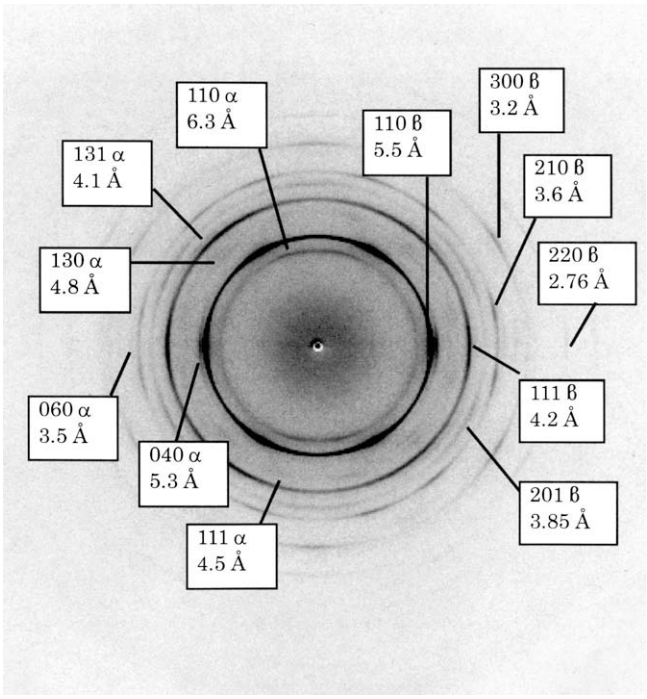

Fig. 8. The EV pattern and the assignments (*hkl* indices and the *d* spacing) of the α reflections (left) and the β reflections (right).

The *d* spacings were elucidated by the monoclinic unit cell with the standard dimensions [46] $a = 6.65$ Å, $b = 20.96$ Å, $c = 6.49$ Å, $\beta = 99.3°$ for the α reflections, and by the three-chain trigonal unit cell (isochiral-domain model) [47] with $a = b = 11.0$ Å, $c = 6.49$ Å, $\gamma = 120°$ for the β reflections. The three isochiral helices assume a frustrated packing, namely, there is no crystallographic symmetry among them [48]. The helices assume the fractional positions at (x, y) = (0, 0), (1/3, 2/3), and (2/3, 1/3) in the trigonal unit cell. Namely, the chain arrangement holds the one-chain pseudohexagonal subcell structure with $a' = 6.37$ Å. This was confirmed by the fact that the main reflections were assigned to the indices of $h - k = 3n$. Fig. 9 shows the diffraction curve transformed from the data of the TV pattern and corrected for the Lorentz and polarization (*Lp*) factors. The α reflections are indicated by arrows. The peaks were separated over the amorphous background scattering (Bg), that

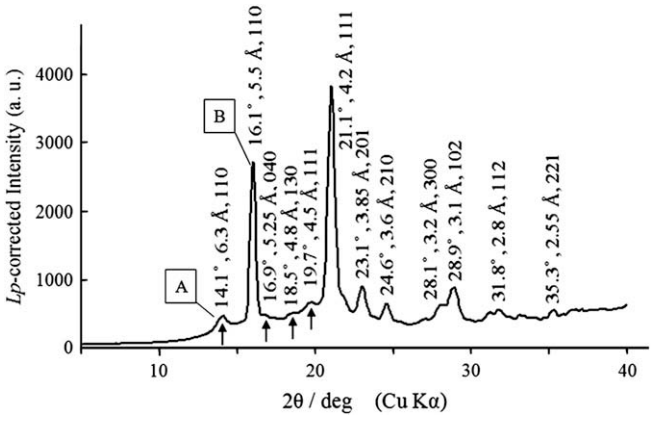

Fig. 9. The *Lp*-corrected XRD curve extracted from the TV pattern, and the assignments of the reflections which are indicated by the 2θ angle, *d* spacing, and the *hkl* indices. The reflections indicated by arrows are attributed to the α-form and the others to the β-form. The reflections A and B are those shown in Fig. 1.

was approximated by a smooth spline curve. The integrated intensity ratio was nearly α:β:Bg ≈ 5:45:50. The same ratio was obtained for the curve extracted from the EV pattern. In spite of the small 2θ range, it may represent the existence ratio.

In Fig. 9, the weak reflection A arises from the (110) faces of the monoclinic α crystals, while the strong reflection B arises from the {110} of the trigonal β crystals, including symmetrically equivalent (210) and (120) faces. The integral widths $\Delta(2\theta)$ of the reflections A and B were about 0.9° and 0.4°, indicating that the sizes (coherent lengths) of the α and β crystals are about 100 Å, and 220 Å, respectively.

The features of the diffraction patterns claim the preferred orientations of the α and β crystals. The reflections A and B are also designated in patterns of Fig. 1. In their respective narrow 2θ ranges, the pixel intensities of the TV pattern were collected and plotted against the azimuthal angle φ defined on the IP plate. The angle φ is associated with the azimuthal angle φ_M pointing to the lattice direction [*hkl*], which is defined to be normal to the corresponding (*hkl*) crystal face. In the case of the normal incidence of X-ray beam to the flat IP, the angles are related by

$$\cos\varphi_M = \cos\theta\cos\phi \quad (1)$$

we describe the direction [*hkl*] by the angles φ_M, φ_N, and φ_T toward MD, ND, and TD, respectively, as shown in the lower left of Fig. 1. The data observed in the TV, EV, and DV patterns are limited to particular intersections of the Ewald sphere (reciprocal space) permitted by the Bragg condition, and are contributed only from a fraction of crystals with the corresponding direction [*hkl*] forming an angle $\pi/2 + \theta$ with the incident X-ray direction. Allowing for the incomplete data, the azimuthal intensity distributions vs. ϕ were transformed into those vs. φ_M (Fig. 10).

The intensity distribution of the reflection A consists of two broad components of the half width $\Delta\phi = 50$–60°; one is around $\varphi_M \approx 0°$ (V component) and the other is around 90° (P component). The former intensity is about twice of the latter. In the EV pattern (Fig. 8), the reflection A appears at $\phi \approx 15°$ and the 040 reflection at $\phi = 90°$ in a narrow range. Therefore, the V-component α crystals orient preferentially with *b*-axis in the ND direction, a^*-axis in the MD direction, and *c*-axis in the TD direction. For *b*-axis, $\varphi_M \cong 90°$ (narrow), while $\varphi_N \approx 0°$ and $\varphi_T \approx 90°$ (broad). For a^*-axis, $\varphi_N \cong 90°$ (narrow), while $\varphi_M \approx 0°$ and $\varphi_T \approx 90°$ (broad).

As mentioned below, the *b*-axis direction ([010]) of the V component was parallel to [110] of β crystals, and the manner of the mutual orientation was very similar. In the limit-ordered α crystal, the four types of chains, up- and down-pointing right-handed and left-handed helices, are engaged in the $P2_1/c$ unit cell. The disordered modification ($C2/c$) involves the up/down disorder [49,50]. Isotactic PP chain can assume both the right- and left-handed

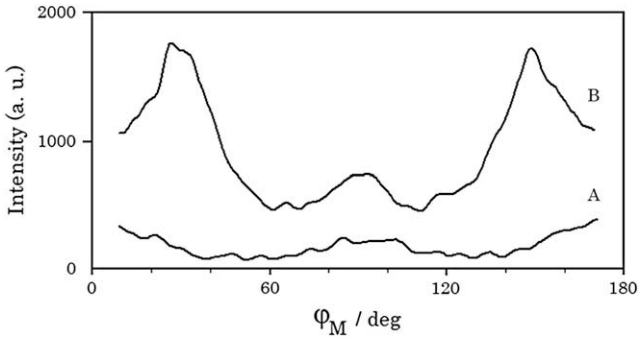

Fig. 10. Azimuthal intensity distributions of the reflections A (α) and B (β) vs. φ_M in the TV pattern.

helical conformations, but the helical rewinding reverses the up–down direction. Essentially, the α-forming arrangements of the right- and left-handed helices are not achieved in β-form, but such arrangements may happen sporadically in small areas, and form less-ordered α crystals. There is a possibility that the V-component α crystals may grow secondarily in the crystallization process of β-form.

The reflection A observed in the DV pattern (the lower right of Fig. 1) is associated with the component P, and its azimuthal intensity distribution is almost uniform. Therefore, the P-component α crystals seem to have the uniaxial orientation with the chain axis parallel to the MD direction, and may grow in a minimum quantity by the shear-induced crystallization in the extrusion process.

On the other hand, the intensity maxima of the reflection B appear at $\varphi_M \approx 30^\circ$, 90°, and 150° (Fig. 10) in the TV pattern. As shown in Fig. 8, the reflection B comprises well-defined six spots in the EV pattern. In the scheme of the axial setting in which the equatorial spot at $\phi = 90^\circ$ (in the ND direction) is assigned to 110, the spots at $\phi \approx 30^\circ$ and 150° are ascribed to $\bar{1}20$ or $2\bar{1}0$. For the direction [110], $\varphi_M \approx 90^\circ$ (narrow), while $\varphi_N \approx 0^\circ$ and $\varphi_T \approx 90^\circ$ (broad). The *c*-axis orients preferentially in the TD direction. Compared to the EV pattern, the broad azimuthal intensity distribution of the reflection B in the TV pattern suggests the small twisting of the β crystals about the [110] axis. From these features, a new morphology depicted in Fig. 11 is proposed. The growth direction is along the horizontal [110] [48]. The intensity distributions in the DV pattern indicate the [110] orients broadly ($\Delta\phi \approx 50^\circ$) in the ND direction. However, there are still some amounts of the β crystals having the [110] in the TD direction, which may give rise to the small maximum at $\varphi_M \approx 90^\circ$ in the TV pattern. There was no particular evidence for the β crystals with the chain axis aligned in the MD direction.

3.3. Mechanical properties

Trouser tear test was performed at room temperature employing two types of the sheet sample containing NU-100; one has a parallel notch to the flow direction (MD), and the other has a vertical notch (TD) as illustrated in Fig. 2. Fig. 12 shows TPR, tear-propagation resistance, is plotted against the displacement. It should be noted that the MD sample shows ductile behavior whereas the fracture occurs in a brittle manner for the TD sample, which is attributed to the unique molecular orientation of iPP. This mechanical anisotropy is completely different from that of conventional polymer products processed by various processing techniques such as fiber-spinning, film, sheet, blow-molding, and injection-molding.

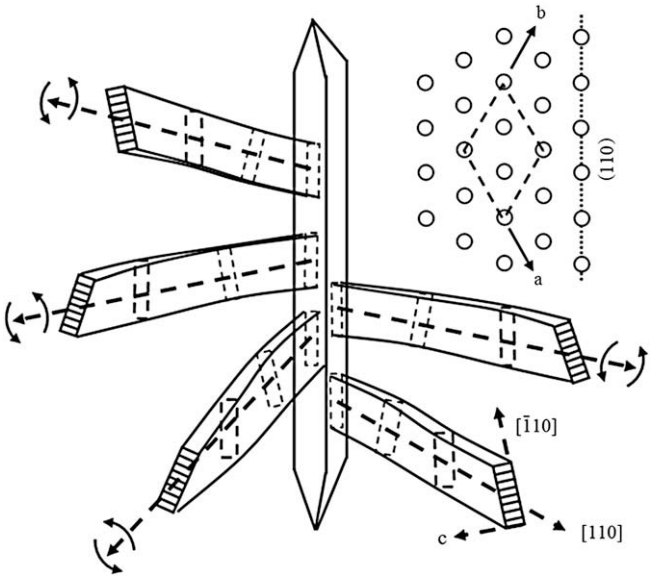

Fig. 11. Crystallization mechanism of β-form iPP on the needle crystals of NU-100 and the stem packing.

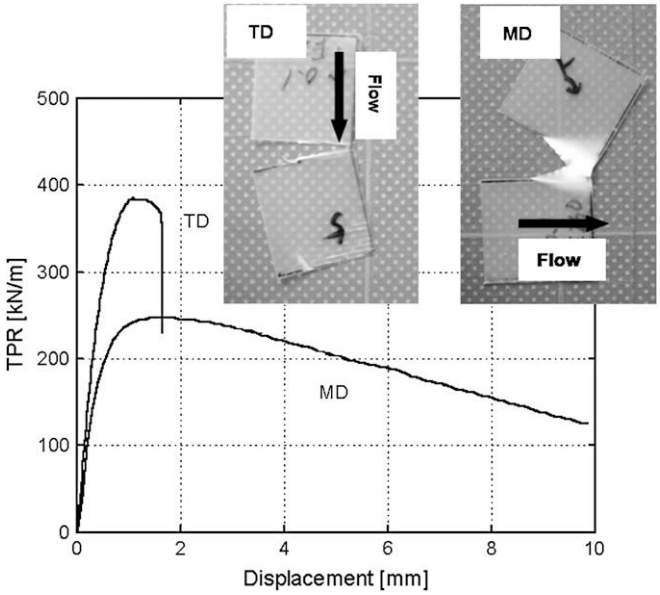

Fig. 12. Tear-propagation resistance (TPR) is plotted against the displacement for MD and TD samples. The fractured samples were shown in the figure.

Furthermore, the appearance of the fractured samples is also significantly different as shown in the figure. The MD sample exhibits a marked stress-whitening behavior with a large plastic deformation area. On the contrary, the brittle failure occurs in the TD sample. The experimental results suggest the possibility to control the direction of the crack propagation.

In the case of iPP, both MD and TD samples exhibit brittle fracture (but not presented here). The difference between the MD and TD samples is not detected because both samples are so brittle.

4. Conclusion

Structure and properties of iPP containing NU-100, as a β-form nucleating agent, were studied employing the sheet samples extruded from a conventional T-die. It is found that dissolved NU-100 appears as needle crystals in a molten iPP. Further, the long axis of the needle crystals orient along to the flow direction. Then iPP molecules crystallize on the surface of the needle crystals, in which *c*-axis of iPP chains orients perpendicular to the long axis of the needle crystals. XRD characterization revealed that there are both α and β forms in the sheet sample with an intense fashion of the β-form. Furthermore, *c*-axis of iPP molecules orients perpendicular to the flow direction, which corresponds with the birefringence measurement. Although NU-100 has been known as a unique nucleating agent providing a wide variety of crystal structures, this is the first report on the transversal orientation of iPP chains. Finally, the anomalous molecular orientation affects the mechanical anisotropy to a great extent. The sample shows ductile behavior in the TD direction, whereas it fractures in a brittle manner in the MD direction.

Acknowledgements

This work was partly supported by Grants-in Aid for Scientific Research (C) (No. 16550173) from the Ministry of Education, Science, Sports, and Culture of Japan.

References

[1] Padden FJ, Keith HD. J Appl Phys 1959;30:1479.
[2] Turner-Jones A, Aizlewood JM, Beckett DR. Makromol Chem 1964;75:134.
[3] Varga J. J Macromol Sci Phys 2002;B41:1121.
[4] Leugering HJ. Makromol Chem 1967;109:204.
[5] Fujiyama M. Int Polym Process 1996;11:271.
[6] Mubarak Z, Martin PJ, Harkin-Jones E. Plast Rubber Composites 2000;29:307.
[7] Huang MR, Li XG, Fang BR. J Appl Polym Sci 1995;56:1323.
[8] Broda J. Polymer 2003;44:6943.
[9] Shi G, Zhang X, Qiu Z. Macromol Chem 1992;193:583.
[10] Varga J, Mudra I, Ehrenstein GW. J Appl Polym Sci 1999;74:2357.
[11] Li X, Hu K, Li M, Huang Y, Zhou G. J Appl Polym Sci 2002;86:633.
[12] Chu F, Yamaoka T, Kimura Y. Polymer 1995;36:2523.
[13] Kawai T, Iijima R, Yamamoto Y, Kimura T. J Phys Chem B 2001;105:8077.
[14] Kawai T, Iijima R, Yamamoto Y, Kimura T. Polymer 2002;43:7301.
[15] Bohaty P, Vlach B, Seidler S, Koch T, Nezbedova E. J Macromol Sci B 2002;41:657.
[16] Cho K, Saheb DN, Yang CH. Polymer 2002;43:1407.
[17] Marco C, Gomez MA, Ellis G, Arribas JM. J Appl Polym Sci 2002;86:531.
[18] Kotek J, Raab M, Baldrian J, Grellmann W. J Appl Polym Sci 2002;85:1174.
[19] Kotek J, Kelnar I, Baldrian J, Raab M. Eur Polym J 2004;40:679.
[20] Zhou J, Liu G, Yan S, Dong J, Li L, Chan C, et al. Polymer 2005;46:4077.
[21] Hou W, Liu G, Zhou J, Gao X, Li Y, Li L, et al. Colloid Polym Sci 2006;285:11.
[22] Menyhard A, Varga J, Molnar G. J Therm Anal Calorim 2006;83:625.
[23] Behrendt N, Mohmeyer N, Hillenbrand J, Klaiber M, Zhang X, Sessler GM, et al. J Appl Polym Sci 2006;99:650.
[24] Varga J, Menyhard A. Macromolecules 2007;40:2422.
[25] Fujiwara Y. Colloid Polym Sci 1975;253:273.
[26] Lovinger AJ, Chua JO, Gryte CC. J Polym Sci Polym Phys Ed 1977;15:641.
[27] Aboufaraj M, Ulrich B, Dahoum A, G'Sell C. Polymer 1993;34:4817.
[28] Dragaum H, Muschik HJ. J Polym Sci Polym Phys Ed 1977;15:1779.
[29] Varga J, Karger-Kocsis J. J Polym Sci Polym Phys Ed 1996;34:657.
[30] Somani RH, Hsiao BS, Nogales A, Srinivas S, Tsou AH, Sics I. Macromolecules 2000;33:9385.
[31] Devaux SE, Chabert B. Polym Commun 1991;32:464.
[32] Zhang J, Shen KZ, Na S, Fu Q. J Polym Sci Polym Phys Ed 2004;42:2385.
[33] Asano T, Fujiwara Y. Polymer 1978;19:99.
[34] Varga J. J Therm Anal 1989;35:1891.
[35] Karger-Kocsis J, Varga J. J Appl Polym Sci 1996;62:291.
[36] Karger-Kocsis J. Polym Bull 1996;36:229.
[37] Karger-Kocsis J. Polym Eng Sci 1996;36:203.
[38] Li JX, Cheung WL, Chan CM. Polymer 1999;40:2089.
[39] Huy TA, Adhikari R, Lüpke T, Henning S, Michler GH. J Polym Sci Polym Phys Ed 2004;42:4478.
[40] Lezak E, Bartczak Z, Galeski A. Polymer 2006;47:8562.
[41] Tenma M, Yamaguchi M. Polym Eng Sci 2007;47:1441.
[42] Tenma M, Mieda N, Takamatsu S, Yamaguchi M. J Polym Sci Polym Phys Ed 2008;46:41.
[43] Masuko T, Tanaka H, Okajima S. J Polym Sci A-2 1970;8:1565.
[44] Russo R, Vittoria V. J Appl Polym Sci 1996;60:955.
[45] Uchiyama Y, Iwasaki S, Ueoka C, Fukui T, Okamoto K, Yamaguchi M. J Polym Sci Polym Phys Ed, 2009;47:424.
[46] Brandrup I, Immergut EH, Grulke EA, editors. Polymer handbook. 4th ed. New York: Wiley-Interscience Pub.; 1999.
[47] Meille SV, Ferro DR, Brückner S, Lovinger AJ, Padden FJ. Macromolecules 1994;27:2615.
[48] Dorset DL, McCourt MP, Kopp S, Schumacher M, Okihara T, Lotz B. Polymer 1998;39:6331.
[49] Hikosaka M, Seto T. Polym J 1973;5:111.
[50] Auriemma F, de Ballesteros OR, de Rosa D, Corradini P. Macromolecules 2000;33:8764.